

# Experimental demonstration of the slow group velocity of light in two-dimensional coupled photonic crystal microcavity arrays

Hatice Altug<sup>a)</sup> and Jelena Vučković<sup>b)</sup>

Edward L. Ginzton Laboratory, Stanford University, Stanford, California 94305-4088

(Received 18 June 2004; accepted 3 February 2005; published online 7 March 2005)

We recently proposed two-dimensional coupled photonic crystal microcavity arrays as a route to achieve a slow-group velocity of light (flat band) in all crystal directions. In this letter we present the experimental demonstration of such structures with a measured group velocity below  $0.008c$  and discuss the feasibility of applications such as low-threshold photonic crystal lasers with increased output powers, optical delay components, and sensors. © 2005 American Institute of Physics. [DOI: 10.1063/1.1882755]

One-dimensional coupled resonator optical waveguides (1D CROWs) were proposed by Yariv *et al.*<sup>1</sup> and subsequently demonstrated experimentally in microwave and optical domains.<sup>2-5</sup> 1D CROWs attracted significant attention because of their ability to provide a very small group velocity of light in the direction in which the cavities are coupled. As in the case of photonic crystal (PhC) waveguides, the coupling into such structures is difficult, since the input beam needs to be aligned in one particular direction and coupled efficiently into a cross-sectional area that is typically much smaller than  $1 \mu\text{m}^2$ . Similarly, PhC microcavity lasers have been studied by many groups because of their small size, low threshold, and possibility of high direct modulation rate;<sup>6-9</sup> unfortunately, their output powers are very low for most applications.

We have recently proposed two-dimensional coupled photonic crystal resonator arrays (2D CPCRA), which enable a small group velocity of light for all wave vectors and in all crystal directions with a very low group velocity dispersion.<sup>10</sup> Our design overcomes the noted disadvantages of 1D CROWs: since a small group velocity occurs in all propagation directions, the coupling into the structure is thus not as difficult. Moreover, when the structure is combined with an active material and employed as a laser, a much higher output power can be achieved than in PhC microcavity lasers, while preserving a low threshold and a high-direct modulation rate. The high density of optical states in such structures can also be used to study nonlinear optics at low thresholds, or to construct compact polarizing optical elements and sensors.

A 2D CPCRA is formed by tiling microcavities in two dimensions, as shown in Fig. 1(b). When combined into a two-dimensional network, defect modes of individual cavities form coupled defect bands located inside the photonic band gap.<sup>10</sup> In particular, the coupled arrays in the square lattice photonic crystal exhibit three coupled TE-like bands: monopole, dipole, and quadrupole.<sup>10</sup> The coupled monopole band is close to the air band edge and is not flat; this band is also outside the wavelength range probed in our experiments and thus is not studied in this letter. Instead we focus on the

coupled dipole and quadrupole bands to obtain the dispersion diagram, and the  $z$ -components of the magnetic field of these modes at the center of the PhC slab is shown in the insets of Figs. 2 and 3, respectively. The coupled dipole bands originate from the doubly degenerate dipole mode; two subbands corresponding to the coupled  $x$ - and the  $y$ -dipoles split away from the  $\Gamma$  point in the  $\Gamma X$  direction, while one degenerate diagonal dipole band is observed in the  $\Gamma M$  direction. Because of the preferential radiation directions for the dipole mode, the coupled dipole bands exhibit different group velocities in different crystal directions. Conversely, the coupled quadrupole band exhibits a small group velocity in all crystal directions, as it originates from the nondegenerate quadrupole mode with a large in-plane  $Q$ -factor and with a fourfold symmetric radiation pattern. In this letter, we also address the effect of small imperfections in fabrication of photonic crystals on degenerate dipole modes.

The designed 2D CPCRA were fabricated in a silicon on insulator (SOI), as described in our earlier publication,<sup>10</sup> and scanning electron microscope (SEM) images of the fabricated structures are shown in Fig. 1(b). For the experiments presented here, a low-index silicon-dioxide ( $\text{SiO}_2$ ) layer underneath the silicon (Si) membranes was not undercut. The presence of the  $\text{SiO}_2$  layer redshifts resonance frequencies and mixes the TE and TM polarizations, but does not affect the slope of the bands significantly, as confirmed by 3D finite-difference time domain (FDTD) simulations. The pa-

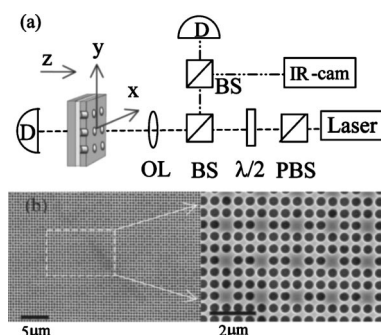


FIG. 1. (a) Experimental setup used in measurement of the CPCRA band diagram. The explanation of symbols is as follows:  $\lambda/2$ : half-wave plate, BS: beam splitter, PBS: polarizing beam splitter, OL: objective lens, IR-cam: infrared camera, and D: detector. Rotations of the structure around the  $y$ - and  $z$ -axes are controlled by two rotation stages; (b) SEM images of the fabricated CPCRA with  $A=3a$ .

<sup>a)</sup> Also at the Department of Applied Physics, Stanford University, Stanford, CA 94305; electronic mail: altug@stanford.edu

<sup>b)</sup> Also at the Department of Electrical Engineering, Stanford University, Stanford, CA 94305; electronic mail: jela@stanford.edu

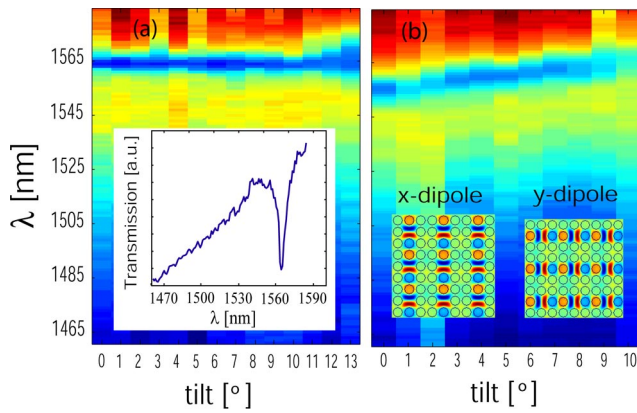


FIG. 2. (Color online) (a) Measured band diagram (from the transmission spectrum) of the CPCRA from Fig. 1 for the coupled  $x$ -dipole mode in the  $\Gamma X$  direction. The dark blue stripe is the location of the coupled band. The horizontal axis is the tilt angle around the  $y$ -axis, which corresponds to different  $k_x$ -values; the vertical axis is the wavelength. The inset shows the transmission spectrum at  $0^\circ$  tilt, i.e., at the  $\Gamma$  point. (b) The measured band diagram for coupled  $y$ -dipole mode. The insets show the magnetic field ( $B_z$ ) pattern of the  $x$ - and  $y$ -dipole mode at the  $X$ -point.

rameters of the fabricated structures are: the PhC periodicity  $a=490$  nm, the hole radius  $r=190$  nm, the slab thickness  $d=275$  nm, and the CPCRA unit cell dimensions  $A \times A=3a \times 3a$  (i.e., two PhC layers are inserted between tiled microcavities). The experimental setup used in the measurement of the dispersion diagram is shown in Fig. 1(a). The structure is excited by a tunable laser source with a scanning range of 1460–1580 nm. The beam is slightly focused on the sample by a very low numerical aperture (NA) objective lens, so that the excitation can be approximated by a plane wave; this is important for the control of the in-plane wave vector ( $\mathbf{k}$ -vector). The size of the device is  $100 \mu\text{m} \times 100 \mu\text{m}$  and the pump beam has the diameter of  $120 \mu\text{m}$  at the sample surface. Polarizing optics are employed to preferentially excite TE-like (even) modes of the structure. We have tested both transmission and reflection spectra of the structure with the same and opposite polarization relative to the pump laser. The employed method for measuring the dispersion diagram is similar to the surface coupling reflectivity technique that uses a white light source.<sup>5,11</sup> The in-plane  $\mathbf{k}$ -vector and the choice of the PhC symmetry direction ( $\Gamma X$  or  $\Gamma M$ ) are controlled by rotating the structure around the  $y$ - and  $z$ -axes, respectively. In order to position the pump beam relative to the device, its reflection is imaged; therefore, the maximum tilt angle that can be tested (before losing the image) is determined by the collection optics and is equal to  $13^\circ$ . However, this is sufficient to probe a relevant portion of the studied CPCRA dispersion diagram, since the tilt angle  $\theta_X$  required to reach the  $X$  point of the two-layer CPCRA is around  $31^\circ$  as estimated from

$$k_{\parallel} = \frac{2\pi}{\lambda} \sin(\theta_X) = \frac{\pi}{3a}$$

and  $a/\lambda \approx 0.3$ . Due to the low NA of the objective lens, the collected reflected signal drops rapidly when the sample tilt around the  $y$ -axis increases; the transmitted signal is thus more convenient for measuring the band diagram. The inset of Fig. 2(a) shows the transmission spectrum of the dipole band at the  $\Gamma$  point (corresponding to the  $0^\circ$  tilt), with the incident beam polarized in the  $x$ -direction, thereby preferentially exciting the  $x$ -dipole. A strong resonance dip near 1564

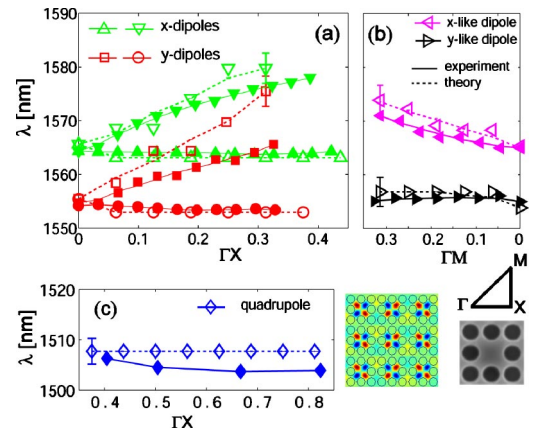


FIG. 3. (Color online) Comparison of the experiment with the FDTD simulations including structural astigmatism and underlying oxide layer. Solid lines with filled markers are experimental results and dashed lines with empty markers are simulation results. The horizontal axis corresponds to the probed fraction of the indicated crystal direction and the vertical axis is the wavelength: (a) dipole bands in the  $\Gamma X$  direction. Triangles and squares denote one set of  $x$ - and  $y$ -dipole bands (also shown in Fig. 2), while inverted triangles and circles denote the other set, obtained after rotating the structure by  $90^\circ$  around the  $z$ -axis; (b)  $x$ - and  $y$ -like dipole bands in the  $\Gamma M$  direction; (c) quadrupole band in the  $\Gamma X$  direction. The middle subfigure shows the magnetic field ( $B_z$ ) pattern of the quadrupole mode at the  $X$  point. The subfigure on the right shows the unit cell and high symmetry directions.

nm can be observed, indicating the spectral position of the mode. By tracking the position of the dip at different tilt angles, we can extract a full band diagram. It should be emphasized that the linewidth of the spectrum is very small (7 nm), even though the signal is transmitted through an array containing 3600 coupled cavities, indicating a high uniformity of the fabricated structures. The 7 nm linewidth corresponds to a quality factor ( $Q$ ) of 220 while for the dipole mode in a single-defect microcavity embedded in a square PhC lattice the simulated  $Q \approx 300$ .

The transmission spectra measured at different tilt angles in the  $\Gamma X$  direction with the pump polarized in the  $x$ - and  $y$ -directions are plotted in Figs. 2(a) and 2(b), respectively. The dark blue stripes located between 1545 and 1565 nm in these figures correspond to the positions of the coupled bands: the flat  $x$ -dipole band [Fig. 2(a)] and the non-flat  $y$ -dipole band [Fig. 2(b)]. We note two discrepancies relative to the theory:<sup>10</sup> first, the  $x$ - and  $y$ -dipole bands do not have the same wavelengths at the  $\Gamma$  point, and second, a different set of  $x$ - and  $y$ -dipole bands is observed when the same set of measurements is performed on the structure rotated by  $90^\circ$  around the  $z$ -axis. These two observations indicate that fabricated structures are not symmetric under  $90^\circ$  rotation. This asymmetry can be noticed in the SEM images of the fabricated structures: structures are slightly astigmatized (as a result of imperfect electron beam lithography), with the hole diameter in the  $x$ -direction larger by roughly 20 nm (5%) than in the  $y$ -direction (the structure periodicity is approximately equal in both directions). The degeneracy of the dipole modes is also lifted in the  $\Gamma M$  direction, where the diagonal dipole splits into  $x$ - and  $y$ -like dipole bands. On the other hand, the quadrupole mode is nondegenerate and the corresponding coupled band does not split into subbands due to structure imperfections. We have studied the structures astigmatized by 6.25% numerically by employing FDTD with discretization of 20 units per  $a$ ; results for dipole bands in the  $\Gamma X$  and  $\Gamma M$  directions are plotted in Figs. 3(a) and Fig. 3(b),

respectively, together with corresponding experimental results (determined by fitting inverted Lorentzians to transmission dips). A very good match between experiment and theory is observed, and the small discrepancy results mainly from a modest FDTD discretization. The wavelength resolutions in the simulation and the experiment are 5.5 and 0.2–1 nm, respectively, and error bar for simulation is indicated in Fig. 3. In order to further justify the identification of the modes, the spectrum at the  $\Gamma$  point is repeated with a broadband source (1200–1700 nm) under  $x$ - and  $y$ -polarized excitation, and it showed the location of both dipole modes, air and dielectric bands, which matches very well with the prediction of simulation (see EPAPS Ref. 12). We have also measured the reflected signal at the opposite polarization relative to the pump laser at the  $\Gamma$ -point. For the  $\Gamma X$  direction with  $x$ -polarized excitation (i.e.,  $x$ -dipole is primarily excited), the signal at the opposite polarization ( $y$ -polarized) shows no peak at the location of the  $x$ -dipole. The lack of a peak at the location of  $x$ -dipole confirms that the studied modes are primarily linearly polarized as expected for dipole modes. In addition, polarizing effects introduced by broken rotational symmetry on degenerate modes have been observed, which is beneficial for polarization control of the CPCRA laser and also important in constructing miniaturized polarizing optics, e.g., a polarizing mirror.

The coupled quadrupole band has not been observed under the plane-wave excitation described above, although theory predicts that it should be in the scanned wavelength range. The reason is that the plane-wave excitation is linearly polarized and uniform in the  $x$ - $y$  plane (at or close to the  $\Gamma$  point), so it cannot excite the quadrupole mode whose electric field has an odd symmetry and an equal presence of the  $E_x$  and  $E_y$  components. In order to approximately locate the position of the quadrupole band, the structure is tilted by about  $20^\circ$  around the  $y$ -axis and the beam is tightly focused; in this case, the excitation field varies in the plane of the structure and is no longer orthogonal to the mode. However, this approach cannot be used to map the quadrupole band accurately, as the  $\mathbf{k}$ -vector information is lost due to the tight focus. The experimental result is shown in Fig. 3(c), and it is very close to the location of the quadrupole band predicted by FDTD simulation. In an active CPCRA device (e.g., a laser containing quantum wells), photons emitted inside the structure can excite modes with arbitrary in-plane symmetry, so the coupling to the quadrupole band would not be a problem.

As can be seen in the simulated and measured band diagrams, the group velocity of the coupled  $x$ -dipole band is small for all wave vectors in the  $\Gamma X$  direction. The measured group velocity at the  $\Gamma$  point is below:

$$V_g|_{\max} = \frac{\Delta\omega}{\Delta k} = \frac{\Delta\lambda}{\lambda} \frac{1}{\Delta\theta} \leq 8 \times 10^{-3}c,$$

where  $\Delta\theta = \pi/180$  is the tilt step in radians,  $\Delta\lambda = 0.2$  nm is the wavelength resolution,  $\lambda = 1564$  nm is the resonance wavelength and  $c$  is the speed of light in vacuum. For optical delay applications, a coupled quadrupole band would be even more suitable, since it exhibits a small group velocity over all  $\mathbf{k}$ -vectors and in all directions.<sup>10</sup> For example, for a symmetric and undercut CPCRA with  $A = 4a$ , we estimate theoretically that the group velocity of the quadrupole band is below  $0.0138c$  and  $0.04c$  in the whole  $\Gamma X$  and  $\Gamma M$  direction, respectively. These results were obtained by fitting co-

sine functions (as predicted for the CPCRA band diagram by the tight binding method<sup>1</sup>) between the quadrupole band frequencies at the high symmetry points ( $\Gamma$ ,  $X$ , and  $M$ ) calculated by the FDTD method.

Finally, we evaluate advantages of a CPCRA laser relative to a PhC microcavity laser. First, its output power would be approximately  $N$  times larger, as it would operate as a phase-locked array of  $N$  microlasers. Second, its electrical pumping would not be as challenging, since approaches similar to those employed in pumping large area PhC band-edge lasers could be used.<sup>13</sup> Last, a pump beam is generally much larger than the cavity size in a PhC microcavity laser, and the majority of the excitons are created in the mirror regions where they cannot couple to the cavity mode, thereby degrading the spontaneous emission coupling factor and the lasing threshold.<sup>14</sup> However, in the CPCRA laser the pump beam overlaps with many cavities, and the wasted pump power is reduced.

In conclusion, we have experimentally demonstrated the band diagram of the 2D CPCRA that we proposed recently<sup>10</sup> and confirmed the existence of flat bands inside the photonic band gap independent of light propagation direction, with measured group velocities below  $0.008c$ . We are currently working on applications of these structures as lasers and sensors.

This work has been supported by the Marco Interconnect Focus Center, and in part by the MURI Center for Photonic Quantum Information Systems (ARO/ARDA Program DAAD19-03-1-0199), the Charles Lee Powell Foundation Faculty Award, and the Terman Award. The authors would like to thank Mehmet F. Yanik for discussion of the experiment, and Dr. Jim McVittie and Eric Perozziello for discussions of dry etching.

- <sup>1</sup>A. Yariv, Y. Xu, R. K. Lee, and A. Scherer, *Opt. Lett.* **24**, 711 (1999).
- <sup>2</sup>M. Bayindir, B. Temelkuran, and E. Ozbay, *Phys. Rev. Lett.* **84**, 2140 (2000).
- <sup>3</sup>S. Olivier, C. Smith, M. Rattier, H. Benisty, C. Weisbuch, T. Krauss, R. Houdre, and U. Oesterle, *Opt. Lett.* **26**, 1019 (2001).
- <sup>4</sup>T. D. Happ, M. Kamp, A. Forchel, J. Gentner, and L. Goldstein, *Appl. Phys. Lett.* **82**, 4 (2003).
- <sup>5</sup>A. D. Bristow, D. M. Whittaker, V. A. Astratov, M. S. Skolnick, A. Tahaoui, T. F. Krauss, M. Hopkinson, M. P. Croucher, and G. A. Gehring, *Phys. Rev. B* **68**, 033303 (2003).
- <sup>6</sup>O. Painter, R. K. Lee, A. Scherer, A. Yariv, J. D. O'Brien, P. D. Dapkus, and I. Kim, *Science* **284**, 1819 (1999).
- <sup>7</sup>J. Hwang, H. Ryu, O. Song, I. Han, H. Song, H. Park, Y. Lee, and D. Jang, *Appl. Phys. Lett.* **76**, 2982 (2000).
- <sup>8</sup>M. Loncar, T. Yoshie, A. Scherer, P. Gogna, and Y. Qiu, *Appl. Phys. Lett.* **81**, 2680 (2003).
- <sup>9</sup>T. Yoshie, M. Loncar, A. Scherer, and Y. Qiu, *Appl. Phys. Lett.* **84**, 3543 (2004).
- <sup>10</sup>H. Altug and J. Vučković, *Appl. Phys. Lett.* **84**, 161 (2004).
- <sup>11</sup>V. N. Astratov, D. M. Whittaker, I. S. Culshaw, R. M. Stevenson, M. S. Skolnick, T. F. Krauss, R. M. De La Rue, *Phys. Rev. B* **60**, R16255, (1999); V. Pacradouni, W. J. Mandeville, A. R. Cowan, P. Paddon, J. F. Young, *ibid.* **62**, 4204, (2000); T. Fujita, Y. Sato, T. Kuitana, and T. Ishihara, *ibid.* **57**, 12428, (1998).
- <sup>12</sup>See EPAPS Document No. E-APPLAB-86-028511 for (brief description). A direct link to this document may be found in the online article's HTML reference section. The document may also be reached via the EPAPS homepage (<http://www.aip.org/pubservs/epaps.html>) or from [ftp.aip.org](ftp://ftp.aip.org) in the directory /epaps/. See the EPAPS homepage for more information.
- <sup>13</sup>S. Noda, M. Yokoyama, M. Imada, A. Chutinan, and M. Mochizuki, *Science* **293**, 1123, (1999).
- <sup>14</sup>H. Ryu, H. Park, Y. Lee, *IEEE J. Sel. Top. Quantum Electron.* **8**, 891 (2002).